Quantifying the effects of gap on the molten pool and porosity formation in laser butt welding

Liping Guo[1,2], Hongze Wang[1,2,3,], Hanjie Liu[1,2], Yuze Huang[4], Qianglong Wei[1,2], Chu Lun Alex Leung[5,6], Yi Wu[1,2,3,*], Haowei Wang[1,2,3]*

1 State Key Laboratory of Metal Matrix Composites, Shanghai Jiao Tong University, Shanghai, 200240, China

2 School of Materials Science & Engineering, Shanghai Jiao Tong University, Shanghai, 200240, China

3 Institute of Alumics Materials, Shanghai Jiao Tong University (Anhui), Huaibei, 235000, China

4 Institute for Advanced Manufacturing and Engineering, Coventry University, CV6 5LZ, UK

5 Department of Mechanical Engineering, University College London, London WC1E 7JE, UK

6 Research Complex at Harwell, Harwell Campus, Oxfordshire OX11 0FA, UK

*Email: Hongze Wang, hz.wang@sjtu.edu.cn; Yi Wu, eagle51@sjtu.edu.cn

Abstract

To obtain a better joint quality in butt welding of aluminum, the gap filling process and the quantification of the gap effects on the molten pool characteristic and the bubble formation were realized by a three-dimensional thermal-mechanistic-fluid coupled model, with the consideration of heat transfer, fluid flow, phase change and recoil pressure. The model was validated by the synchrotron-radiation result. The competition between the solidification and melting at the bottom of the molten pool was uncovered to determine the gap filling process and the molten pool morphology. Gap increased the heat loss, and the molten pool tip was elongated due to gap filling. Four phenomena appeared in sequence in the initial stage of butt welding: I. Gap filling; II. Frozen; III. Remelt; IV. Bubble formation. The result also demonstrated that the gap would disturb the molten pool. In the initial stable growth stage of the molten pool, the larger the gap width, the greater the molten pool depth. The sharp change of keyhole depth was due to the necking formation, while the small fluctuation of keyhole depth with larger gap values resulted from the perturbation by the gap. Bubble formation depends on the degree of the fluid flow and the gap filling due to the unique fluid dropping down phenomenon of butt welding with gap. A continuous melt pool cannot be formed when

the gap width beyond 20 μm, which is detrimental to the welding quality. These findings are of great significance for guiding the optimization of butt-welding process, such as reducing the roughness of the butt interface or increasing the clamping force to reduce the butt gap.

Keywords: simulation; laser butt welding; gap filling; bubble

1. Introduction

Laser butt welding is increasingly adopted in the aerospace, automotive and shipbuilding industries, which uses a moving laser beam as the heat source and joints two parts by melting and solidification [1-3]. The interaction between laser and matter accompanies by the rapid heating and cooling, involving many highly dynamic and transient physical phenomena, such as melting, evaporation, molten metal flow, solidification and non-equilibrium phase changes [4, 5] , during which defects such as pores and spattering may occur. To determine the optimal conditions and improve the welding quality, the molten pool behavior in the welding process needs to be further studied. With the development of science and technology, the in-situ observation method based on X-ray imaging technology is an effective way to obtain the information inside the molten pool [6-9]. A lot of work has been done to investigate the dynamics of keyhole and molten pool, spatter and pore in the laser welding [10-15]. Matsunawa et al. [16] studied the keyhole and molten pool dynamics via the high-speed in-situ X-ray imaging. Heider et al. [13] revealed that the bubble generated at the tip of the capillary is one mechanism to cause welding defects, such as ejections and pores. The increased pressure inside the keyhole promotes it to expand and thus forming spatter. Similar mechanism was also uncovered by Miyagi [10]. Kawahito et al. [11] performed the X-ray imaging of the keyhole and molten pool, and demonstrated that the upward flow in the molten pool behind the keyhole leading to melt ejections.

Nevertheless, most of the in-situ monitoring experiments about the molten-pool dynamic characteristic were conducted on the bead-on-plate welding situation, which is different from the laser butt welding that possesses a gap at the interface. The existing one about laser butt welding is conducted by Wang et al. [17] who observed the melting and filling process by X-ray phase contrast imaging. They revealed two unique features of molten pool, which are different from those of the plate welding. The molten pool and keyhole were initially observed in the position below the upper surface and then expanded upwards and downwards due to gap filling effect. In contrast, the molten pool in laser welding is formed in the upper surface and then grew upwards through heat transfer. The other difference is that there are two boundaries in the laser butt gap welding. However, due to highly transient laser-matter interaction and the limited time resolution of the X-ray contrast method (~1 ms), the specific gap filling process remains challenging to study. Hesse et al. [18] revealed that variation in gap distance during welding would lead to process instability and stress concentrations, which could adversely affect the service properties. It will be of great significance for improving the welding quality to further explore the gap filling process and the effect of the gap on the weld pool characteristics with higher precision.

Numerical simulation is an economical and effective method that has been widely adopted in the research of molten-pool dynamic simulations in the presence of heat transfer and fluid flow [9, 19-27]. Cho et al. [20] investigated the temperature distribution characteristic of weld bead and molten flow by simplifying the multi-phase problem into a single-phase problem using finite volume method (FVM). The fusion zone shape predicted by the simulation result was in good agreement with the experimental fusion zone profile. Ai et al. [23] studied the molten pool and keyhole profile as well as the defect generation during the high-power laser welding by FVM. They revealed that the main factor for spattering formation is the column and swelling in the oscillation interface between melt pool and keyhole. Li et al. [22] carried out research on the keyhole evolution and molten metal flow under different sub-atmospheric pressures in the laser welding of aluminum based on the FVM. They demonstrated that the larger keyhole opening and larger melt flow velocity under a lower pressure is responsible for the reduction of porosity. Leung et al [9] also revealed that the pore and keyhole formation mechanisms are driven by the mixing of high temperatures and high metal vapor concentrations in the keyhole using a combination of in situ X-ray imaging and high-fidelity multiphase simulation.

In this paper, a three-dimensional multi-physics model is established to explore the gap filling mechanism in the laser butt welding of aluminum, with the consideration of heat transfer, fluid flow, recoil pressure, Marangoni effect and solidification drag model. The proposed model is validated against the high-speed synchronous radiation result. We use such model quantified the temperature distribution, fluid flow, as well as the effects of gap on the molten pool characteristic and bubble generation.

2. Mathematical model and numerical simulation

The plates used in the experiment have a high surface finish with surface roughness between 3 μm to 6 μm. Several simulations with different gap values (0 μm, 8 μm, 12μm, 16 μm, 20 μm, 24 μm) were carried out while considering the slight warping phenomenon during the clamping process, where the modelling results with a gap value of 12 μm matched well with that of the experimental tests. Based on these simulations, the effect of different gap values on the joint quality were further explored.

The interaction between high-power laser and material involves many physical phenomena, such as heat transfer, phase change, gas and fluid flow, plume generation, etc. The following assumptions are made to simplify the calculation. (1) Only consider the heat transfer between the material and surrounding environment, while the shielding gas is neglected; (2) The plume and vapor dynamics due to evaporation is ignored, but the recoil pressure is included; (3) The fluid is regarded as incompressible Newtonian fluid with laminar flow. Volume of fluid (VOF) method is adopted to trace the evolution of free surface, in which scalar value F is used to represent the volume fraction of the fluid in a mesh. $0 < F < 1$ denotes the gas-fluid interface.

2.1 Recoil pressure

Evaporation occurs in the area with temperature above boiling point under laser irradiation, accompanied by the recoil pressure exerted in the opposite direction of vapor ejection. It is proportional to the saturation pressure and increases exponentially with the temperature rising. The widely accepted recoil pressure expression is Clausius–Clapeyron equation [28], which is suitable for the situation that ambient pressure has no influence in the evaporation process. In this work, the modified recoil pressure P_r is adopted based on ref. [29] which takes the ambient pressure into consideration, expressed as:

$$P_r = P_s - P_{atm} \tag{1}$$

$$P_s = \begin{cases} P_{atm} & 0 \le T < T_{b1} \\ 0.002726506 * (T - 2606)^2 + 101300 & T_{b1} \le T < T_{b2} \\ \frac{1+\beta_R}{2} P_{atm} exp\left[\frac{L_v(T - T_b)}{TRT_b}\right] & T_{b2} \le T < \infty \end{cases} \tag{2}$$

here P_s is the surface pressure and P_{atm} is the ambient pressure. β_R is the recondensation coefficient and L_v denotes the latent heat of evaporation. T and T_b represent the liquid temperature and boiling point, respectively. R is the universal gas constant. T_{b1} and T_{b2} are defined as $0.95T_b$ and $1.05T_b$, respectively.

2.2 Heat source and boundary conditions

To be consistent with the experimental conditions, the laser beam is operating continuous wave with a wavelength of 1060 nm. It is regarded as Gaussian distribution and a part of the surface heat flux boundary condition [30], described as

$$q = \frac{3PA}{\pi r^2} e^{\left[\frac{-3(x^2+y^2)}{r^2}\right]} \tag{3}$$

where q is the laser heat source, P is the laser power, A is the laser absorptivity value and r is the radius of the laser beam spot. (x, y) is the coordinate of the mesh within the laser irradiation. The algorithm for free-surface tracing is to find the mesh in the free surface under laser irradiation and heat it. After the time step, Δt, it repeats the above step until the calculation is ended. The energy transfer in the upper surface includes evaporation, radiation and convection. It can be expressed as

$$K\frac{\partial T}{\partial \vec{n}} = q - h_c(T - T_a) - \sigma\varepsilon(T^4 - T_a^4) - q_{evap} \tag{4}$$

$$q_{evap} = \varphi L_v P_{atm} \sqrt{\frac{1}{2\pi RT}} exp\left[\frac{L_v(T - T_b)}{TRT_b}\right] \tag{5}$$

For other surfaces, only radiation and convection are considered. The balanced equation is

$$K\frac{\partial T}{\partial \vec{n}} = -h_c(T - T_a) - \sigma\varepsilon(T^4 - T_a^4) \tag{6}$$

Here K is the thermal conductivity and $\vec{n}$ is the normal vector. h_c is the convective coefficient. T_a is the reference temperature and q_{evap} is the heat loss due to evaporation. φ is the accommodation coefficient. ε and σ represent the radiation emissivity and Stefan-Boltzmann constant, respectively. The balanced pressure boundary condition in the upper surface can be expressed by

$$-P + 2\mu\frac{\partial \vec{v}_n}{\partial \vec{n}} = -P_r + \frac{\gamma}{R_k} \tag{7}$$

in which P is the pressure. μ and $\vec{v}_n$ denote the viscosity and the normal velocity vector, respectively. γ is the surface tension and R_k is the radius of surface curvature.

2.3 Computational domain and simulation

The computational domain is shown in **Fig. 1**. In order to improve the computational efficiency without losing the accuracy, the mesh is divided in a non-uniform manner. It is set to be 6 μm along z-axis. The laser beam is located at x=150 μm initially, moving along the positive direction of x-axis. The calculation time is set to be 12 ms. In the region where a keyhole will form, the mesh is finely divided into 6 μm. While out of this range, auto-mesh is applied by setting the mesh counts in a coarse manner to avoid the sharp change of mesh size. The total mesh count is > 2.1 million.

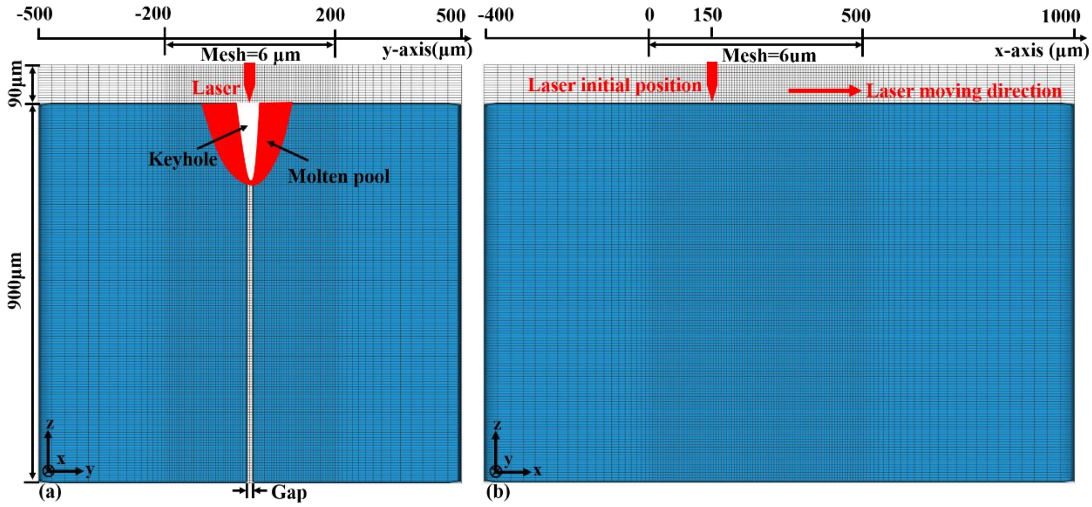

Fig. 1 Computational domain and mesh, (a) the left view, (b) the main view.

The simulation parameters can be found in **Table 1**. Laser power is 500 W and scanning speed is 16.7 mm·s^{-1}. The laser spot diameter is 140 μm. The thermophysical properties for aluminum are shown in **Fig. 2**. The temperature distribution, pressure and velocity in the molten pool can be obtained by solving the momentum conservation, energy conservation and mass conservation equations.

Table 1 Parameters used in this simulation

Properties	Value
Latent heat of evaporation L_v (J· Kg^{-1})	1.077E+07
Gas constant R (J· Kg^{-1}· K^{-1})	308
Saturation pressure P_{atm} (Pa)	101300
Recondensation coefficient β_R	0.5795 [31]
Convective heat transfer h_c (W· m^{-2}· K^{-1})	80
Reference temperature T_a (K)	298
Stefan-Boltzman constant σ (W· m^{-2}· K^{-4})	5.67E-08
Radiation emissivity ε	0.36
Boiling temperature T_b(K)	2750
Melting temperature (K)	933
Absorptivity value A	0.65

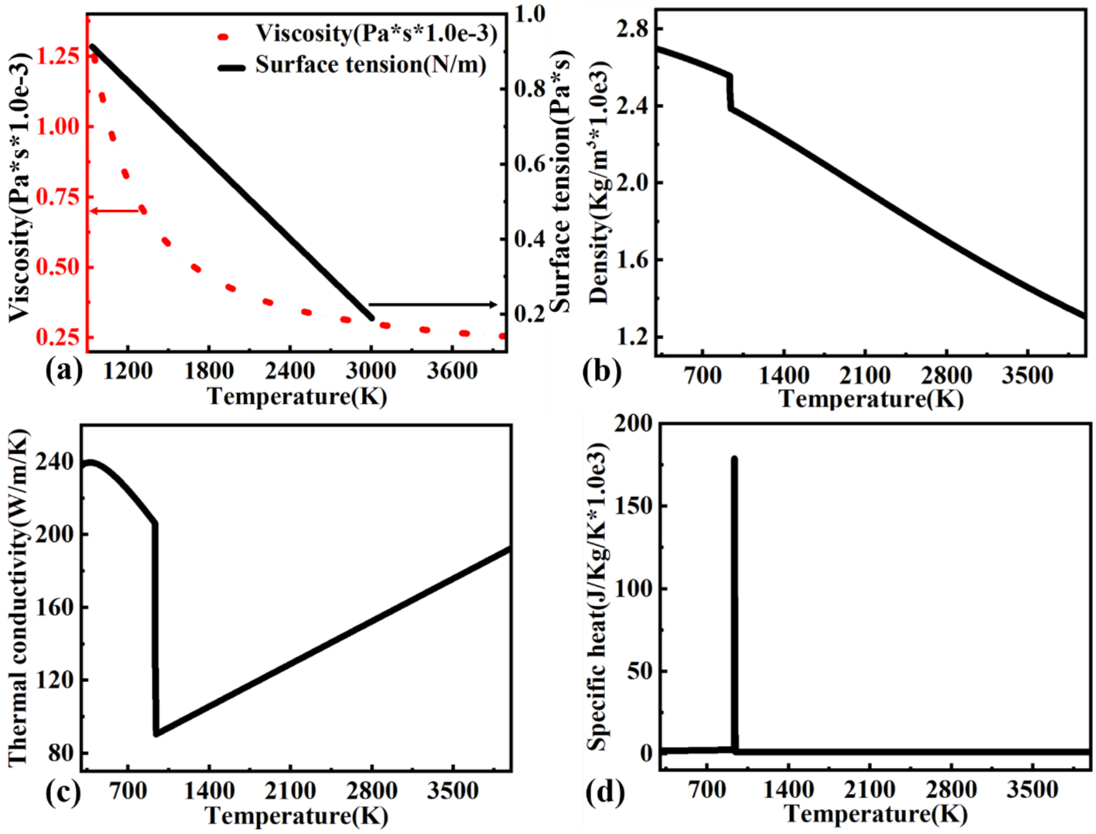

Fig. 2 Thermophysical properties for aluminum used in the simulation [32], (a) viscosity and surface tension, (b) density, (c) thermal conductivity, (d) specific heat.

The model is validated by comparing with the high-speed X-ray imaging results by Wang et al. [17], shown in **Fig. 3**. The simulated molten pool and keyhole morphology (500 W and 16.7 mm·s^{-1}) are similar to those revealed by synchrotron radiations (500 W and 16.7 mm·s^{-1}), which validates the model.

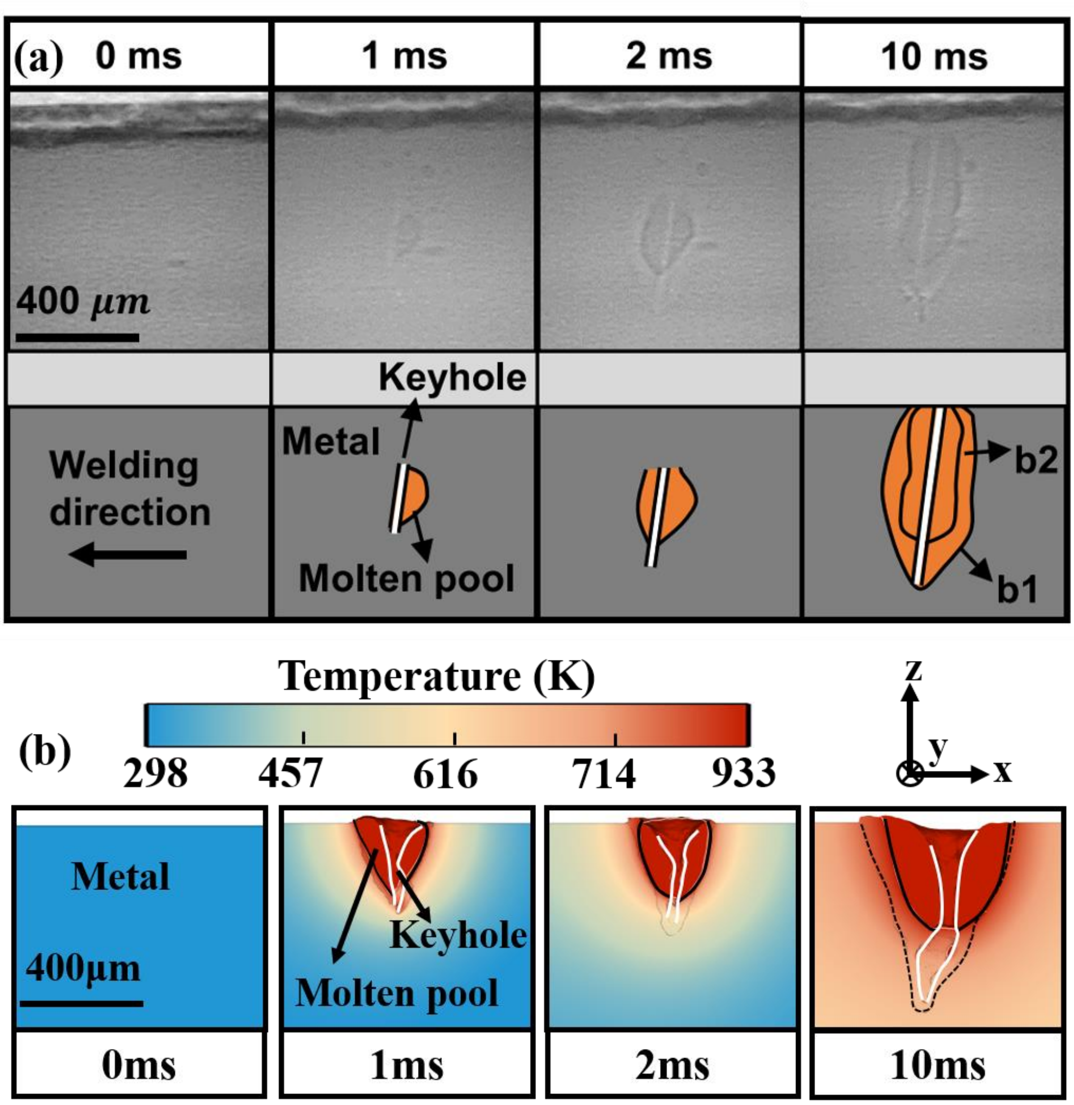

Fig. 3 Simulation model validation, (a) X-ray imaging result (Reprinted from Ref. [17] with permission from Elsevier) and (b) simulation result. The solid white line shows the keyhole outline. The black solid and dotted lines in (b) represent the molten pool boundary and frozen line, respectively.

3. Results and discussion

3.1 Gap filling mechanism

The gap filling process and molten pool evolution are displayed in **Fig. 4**. At the initial stage (0.015 ms), a bridge is generated between two plates. The molten pool morphology initially presents two different ellipses, and the molten depth increases when approaching the gap. We hypothesize that those dynamics are induced by the downward fluid flows, driven by the gravity and recoil pressure, filling the gap. With the heat accumulation, the region adjacent to the gap absorbs much more energy, leading to a triangular pyramid shape of the molten pool (0.021 ms). Under the effect of gap filling, the tip of molten pool is elongated and the corresponding depth rapidly increases. As the gap increases radiation, the fast downward flow reaches a deeper region and leads to a higher heat dissipation, causing fast solidification at the molten pool bottom. The frozen region (0.021 ms) prevents the downward filling, which is controlled by the competition between solidification, melting as well as the filling velocity. When the heat accumulates to a certain extent under the continuous laser irradiation, the frozen part remelts and the fluid continuously flows downward to fill the gap with an elongated tip (0.032 ms). Filling-solidification process repeats several times at the bottom of the molten pool, leading to necking formation in the upper part of the keyhole, blocking part of the laser energy. In the dual role of tip elongated and the necking, the lower part of the molten pool solidifies quickly while the keyhole sidewall is gradually captured by the solidification interface, resulting in a cut-off (0.054 ms). But the bottom can still be irradiated, and the keyhole depth still increases. After that a bridge forms between the rear and front keyhole wall, and a pore is generated at the bottom of laser-matter interaction zone (0.260 ms).

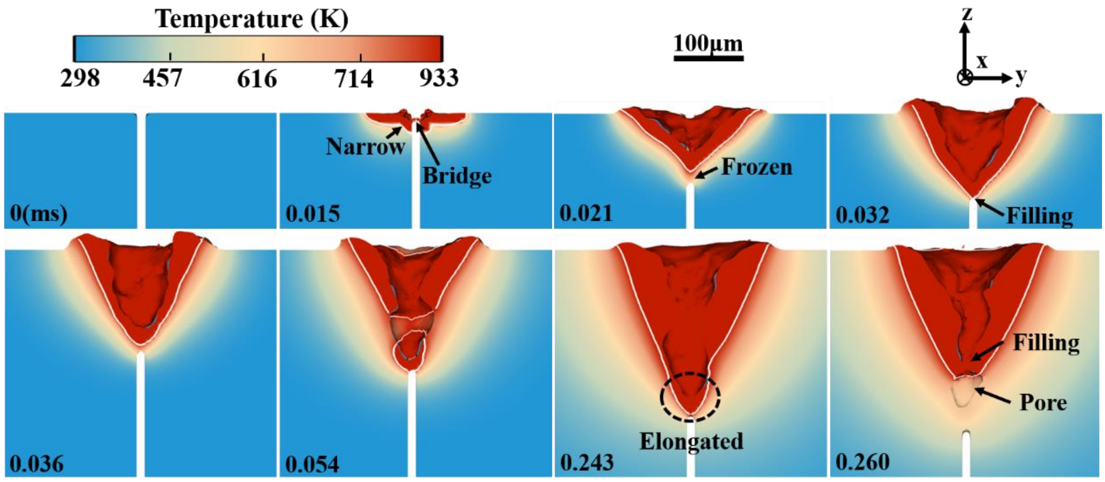

Fig. 4 Evolution of molten pool and the gap filling process in the cross-section (x=150 μm) perpendicular to the laser moving direction. The white lines denote the fusion boundary. The gap distance is 12 μm.

Fig. 5 shows the molten pool evolution and gap filling process in the cross-section view (y=0 μm) parallel to the laser moving direction. A bridge occurs between two plates at 0.015 ms, in which the length of the molten pool is smaller due to the gap filling effect. As the downward flow penetrates to a deeper region in the gap, the rapid radiation and heat conduction promote the fluid solidification and forming a frozen area (0.021 ms). The frozen part stops the fluid from filling the gap and decreases the heat dissipation. The heat accumulated to some specific levels, the solidified region is remelted and the fluid flow downwards to fill the gap (0.032 ms). The filling-solidification process repeats continuously as the fluid flows downward to fill the gap during the expansion of the molten pool. As the keyhole depth grows further, necking is formed at the upper part of the keyhole, increasing the disturbance to the melt pool and keyhole (0.054 ms). At this stage, the keyhole is much more unstable, easily to form a bubble at the bottom (0.257 ms).

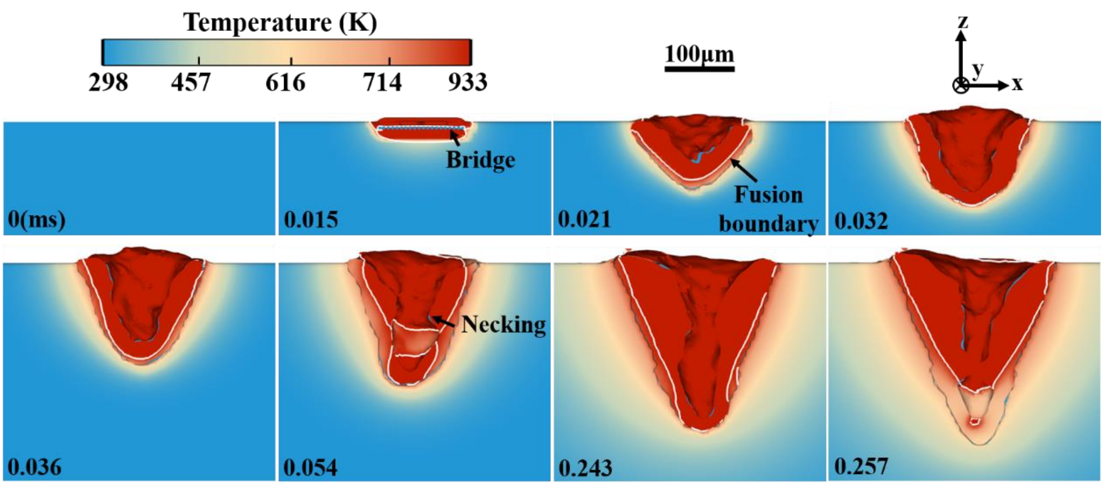

Fig. 5 Evolution of molten pool and the gap filling process in the cross-section parallel to the laser moving direction. These 3D temperature clips are located at y=0 μm (the middle of the gap). The white lines denote the fusion boundary. The gap distance is 12 μm.

The fluid dynamics in the gap are presented in **Fig. 6**. The metal melts under the irradiation of laser, then flows downwards due to the gravity and recoil pressure. The fast heat dissipation at the molten pool bottom causes freezing. Then the fluid flows upward along the rear and front keyhole wall other than downward (0.021 ms). Under the continuous laser irradiation, the frozen part remelts and the molten pool depth increases. The fluid flows radially outward due to the recoil pressure and fills the gap (0.032ms), leading to the elongation of the melt pool tip. By repeating the gap filling-solidification process, the molten region gradually expands. When the keyhole drills down to an unstable state, necking occurs on the keyhole wall, causing fluctuation. The combination of tip elongated effect and necking results in the keyhole sidewall to be captured by the liquid-solid interface while the bottom can still get irradiation and melt (0.054 ms). Then a bridge forms between the rear and front keyhole wall and generates a bubble.

From the above discussion, there are four phenomena appearing in sequence in the initial stage of welding, shown in **Fig. 7**. I. Gap filling: Molten metal forms and the melting velocity exceeds the solidification velocity, the fluid flows downward to fill the gap. II. Frozen: As the fluid flows reaching a certain depth where the heat dissipation is greater than the heat accumulation, namely, the solidification velocity is larger than both the melting and filling velocities, the molten pool bottom solidifies, preventing the downward flow and reducing the heat loss. III. Remelt: As the numerous heat accumulation, the melting process gradually dominates the solidification process, the fluid continuously flows downward and fill the gap. IV. Bubble formation: The filling-solidification process repeats. When the keyhole depth reaches an unstable state, necking occurs and promotes the keyhole fluctuation. Coupled with the tip elongated effect, the bubble is easily generated at the bottom of the keyhole.

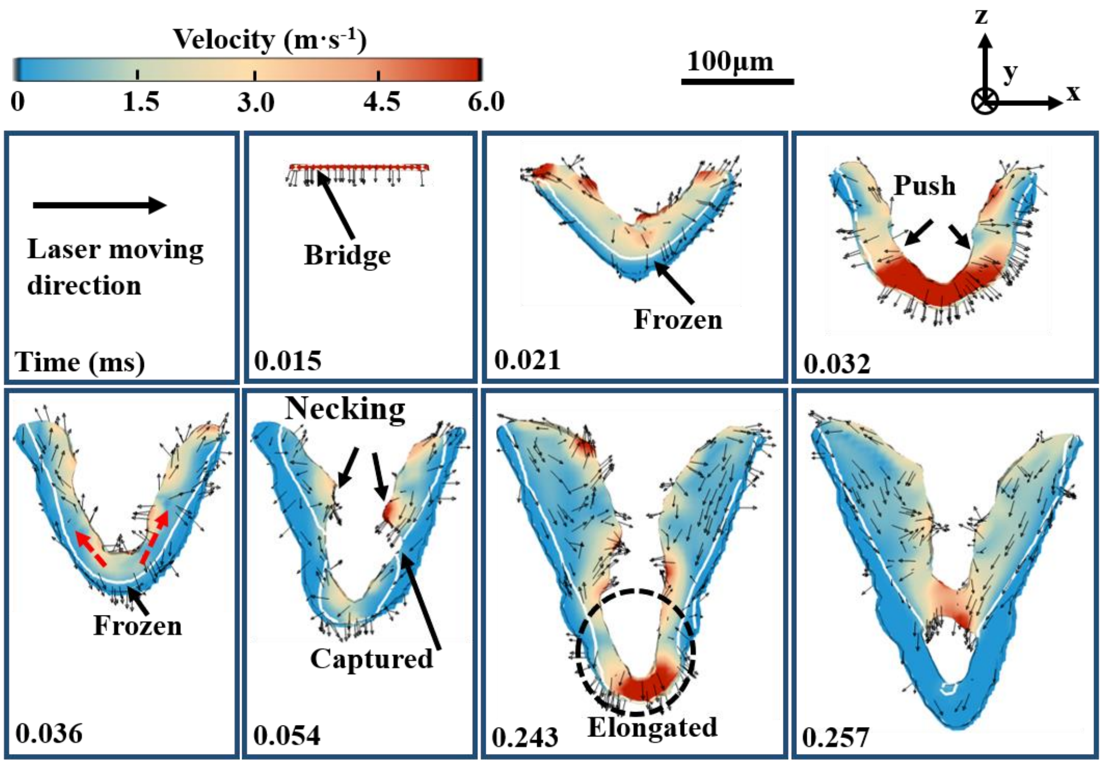

Fig. 6 Snapshots of the fluid flow in the gap. The white lines denote the fusion boundary and the gap width is 12μm.

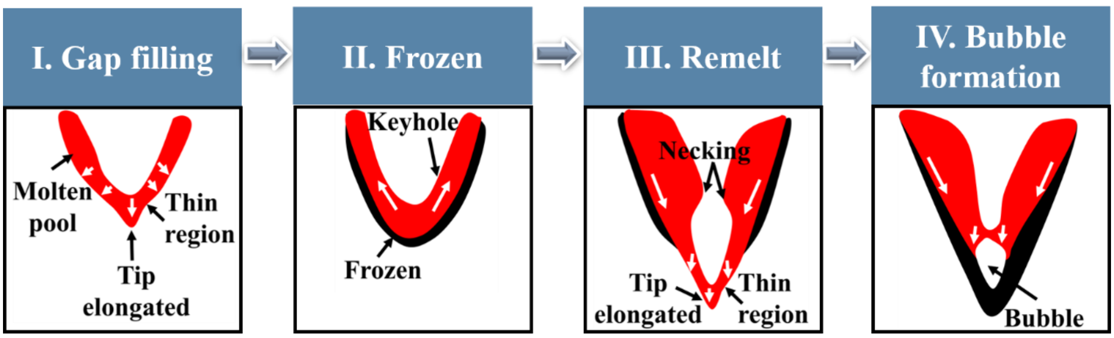

Fig. 7 Four key phenomena in the initial stage of welding. The white arrows denote the fluid direction.

3.2 Influence of gap on the filling process

To explore the effect of gap on the joint quality, models with different gap values are established, and the fluid flow, molten pool evolution and force distribution are analyzed.

The evolution of molten pool and gap filling process are demonstrated in **Fig. 8**. The laser beam moves along the positive direction of the x-axis. The top surface of the material absorbs the laser energy and starts to melt when the temperature exceeds the melting point. A bridge is formed between the two plates due to surface tension, which is in the shape of an arch (0.015 ms). With large gap width, the gravity and recoil force play a dominant role, and the fluid flows downward to fill the gap. The molten pool depth close to the gap is large while that in the region far from the gap is small, and there is a sharp change. The heat energy accumulates and conducts around, causing the molten pool expanding. The surface tension decreases while the recoil force rises exponentially with a higher temperature [33]. Under the effect of gap filling, the tip of the molten pool is elongated, and the larger the gap, the longer it is stretched. Under the same moment, the molten pool depth increases with a larger gap. At the time of 0.021ms, the bottom of the molten pool has solidified in the case with large gap width (12 μm and 16 μm), preventing the gap filling. Under the condition with gap width being 8 μm, no solidification has occurred. This can be attributed to that the larger the gap, the more heat loss by radiation; the deeper the molten pool, and the faster the heat conduction. These combined effects cause the solidification speed to prevail and the freezing occurs. It can be seen at the moment of 0.032 ms that the remelting for the case of 12 μm has priority over the case with 16 μm. This is due to the larger heat dissipation requiring more heat accumulation. While the molten pool depths for the models with gap width 0 and 8 μm gradually increase.

This filling-solidification process repeats and when the keyhole depth exceeds a certain range, necking forms on the keyhole wall, causing fluctuation. Due to the effect of gap filling, the tip of the molten pool is elongated, and the region between the keyhole wall and the fusion boundary becomes thinner. Under the effects of the two, the tip of the molten pool is more unstable and easily forms a bubble [7].

The velocity distribution of the fluid with different gap width is displayed in **Fig. 9**. As laser initially irradiates the material, the keyhole has not been formed and the fluid velocity for the gap width 0 μm is near 0 $m \cdot s^{-1}$ (0.015 ms). The velocity increases with the gap width rising, which can be attributed to more space for the fluid to flow. As the time extends, keyhole gradually appears for the 0 μm case, around which the velocity evenly distributes. While for the cases with a gap exists, the region closer to the gap possess larger velocity due to the gap filling effect that melt drops down. At the moment of 0.021 ms, the solidification dominates at the melt pool bottom for the 12 μm case. Thus, the fluid cannot flow downward and the velocity decreases. For the case of 16 μm, despite the large heat dissipation, the filling effect still dominates the fluid flow due to the large gap width. When it comes to the 0.032 ms, for the cases with small gap values (0 μm and 8 μm), the low velocity leads to the melt pool expanding slowly. When the gap width is 12 μm, the heat accumulation results in the melting and downward filling prevailing. While for the case of 16 μm, the melt pool bottom just starts to solidify, which is later than that of the 12 μm, and the velocity is close to 0 $m \cdot s^{-1}$. At the moment of 0.093ms, the keyhole oscillation causes the bottom of the melt pool to solidify and form pore, preventing the downward flow.

Fig. 10 shows the snapshots of the molten pool morphologies with different gap widths from the top view. In the presence of gap, a bridge occurs between two plates due to the surface tension (0.015 ms). As the temperature increases, the recoil pressure rises exponentially, radially outward. The larger the gap, the more the heat dissipation, resulting in a smaller recoil pressure, which can be seen in **Fig. 11**. In the case of gap width being 8μm, spattering occurs due to the large recoil pressure (**Fig.11** (b)) at 0.019 ms. While for the models with larger gap width, the downward filling coupled with the smaller recoil pressure, no obvious spatter happens. Under the effect gap filling, the molten length is smaller than its width, while for the case with no gap, it is circular in the top view. Actually, the gap filling process is somewhat similar to deep penetration welding, not only the heat dissipation by radiation and conduction, but the direct energy loss as the laser penetrates the plates [34].

In fact, we also explored larger gap width, shown in **Fig. 12**. However, the results reveal that when the gap width exceeds 20 μm, the fluid will fall down during the gap filling process. That is to say, a continuous melt pool will not be formed, which is not conducive to the welding quality. These findings are of great significance for optimizing the butt-welding process. Measures such as reducing the roughness of the butt interface or increasing the clamping force can be adopted to reduce the butt gap and improve the joint quality in the actual laser butt welding process.

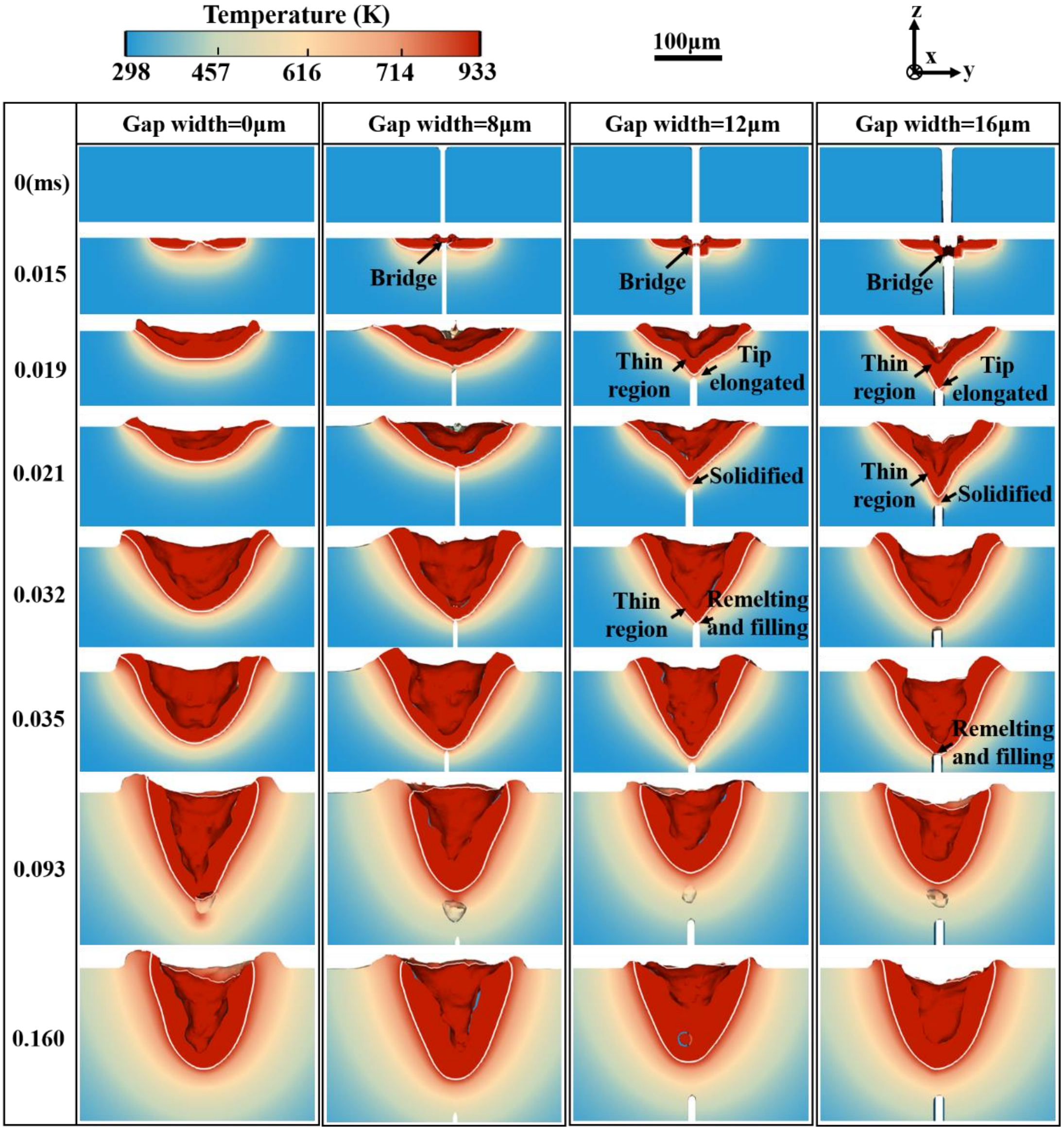

Fig. 8 Evolution of molten pool in the cross-section (x=150 μm) perpendicular to the laser moving direction with different gap values (0 -16 μm). The laser beam moves along the positive direction of x-axis. These 3D temperature clips are located at the middle of the gap.

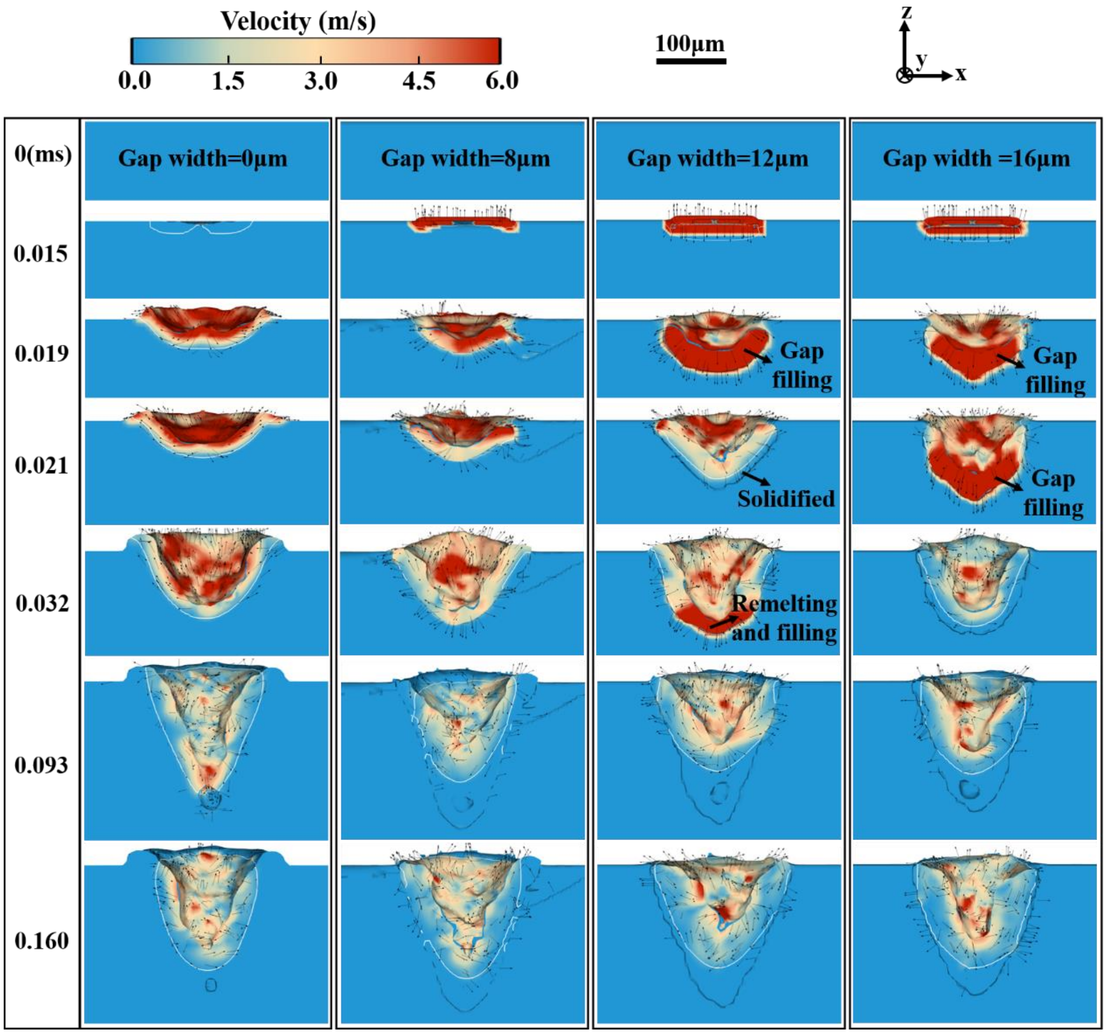

Fig. 9 Evolution of molten pool and the fluid flow in the cross-section (x=150 μm) parallel to the laser moving direction with different gap values (0 -16 μm). The laser beam moves from left to right. These 3D velocity clips are located at the middle of the gap.

330
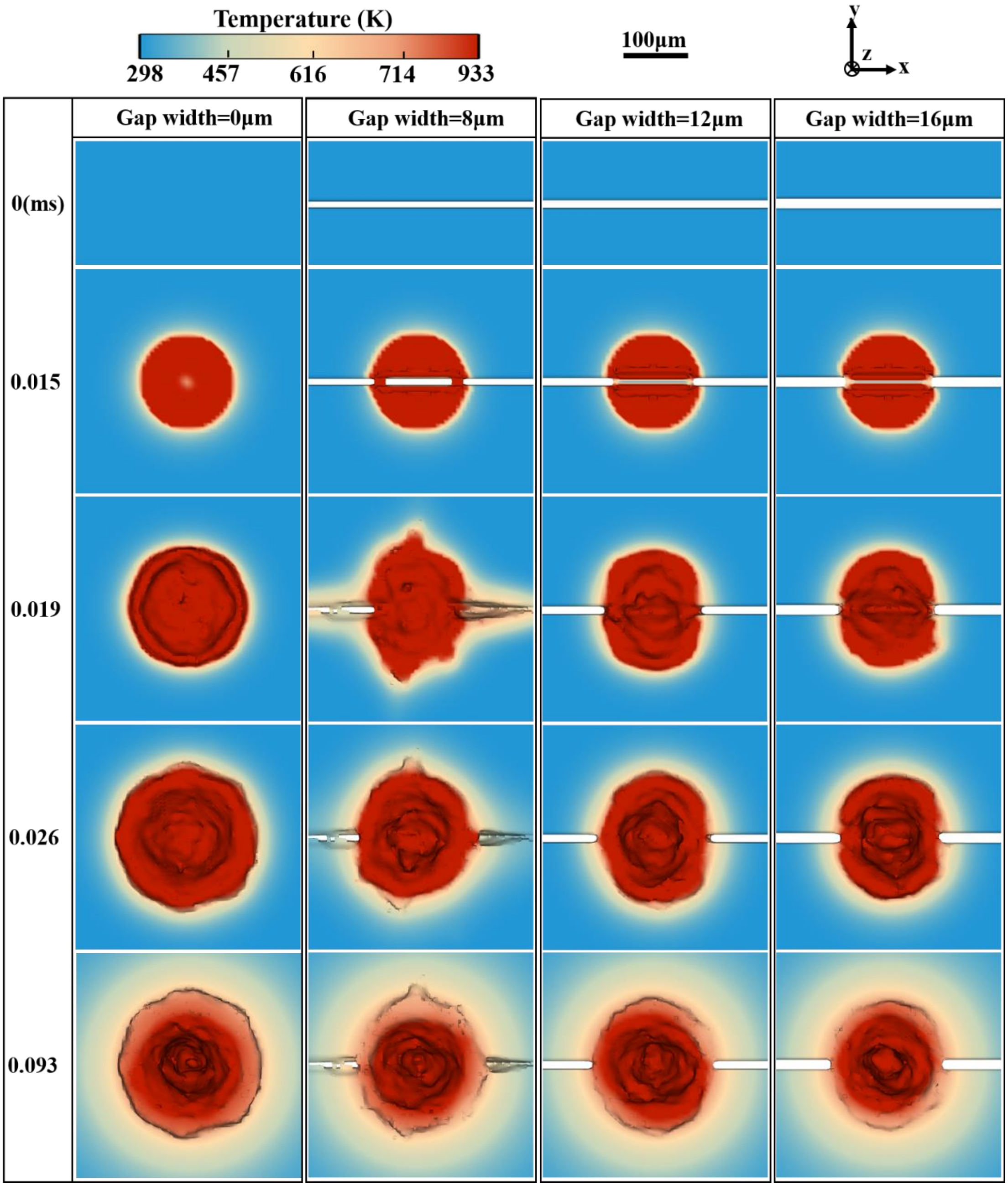

331 **Fig. 10** Snapshots of molten pool morphology form the top view with different gap
332 widths. The laser beam moves from left to right.

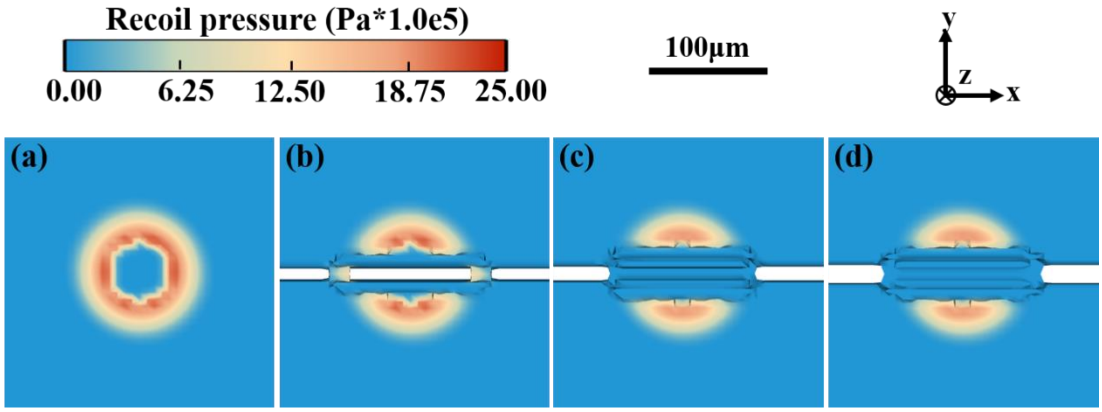

Fig. 11 Distribution of recoil pressure with gap width being (a) 0 μm, (b) 8 μm, (c) 12 μm and (d) 16 μm at 0.019 ms from the top view. The laser beam moves from left to right.

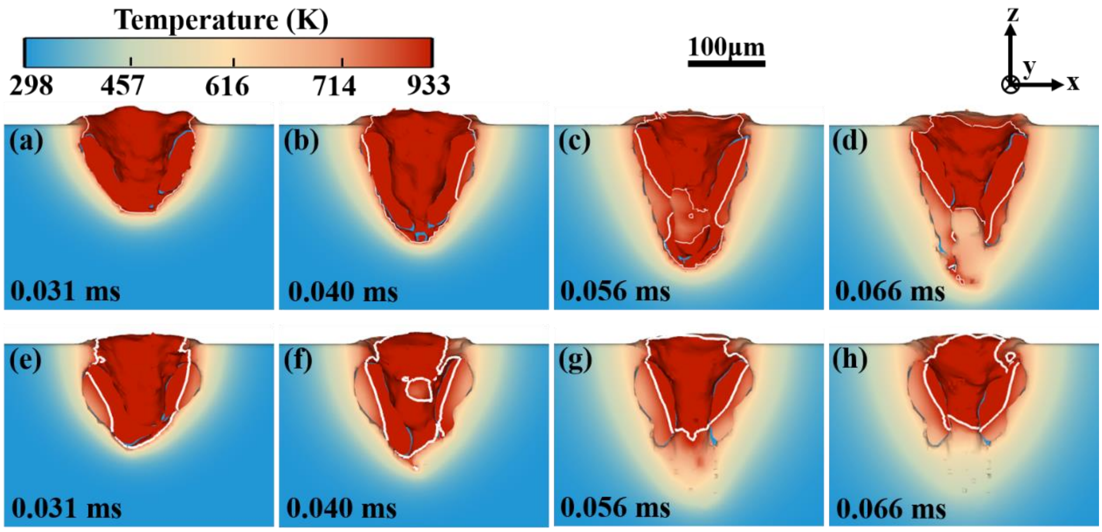

Fig. 12 Evolution of molten pool in the cross-section parallel to the laser moving direction with gap width (a-d) 20 μm and (e-f) 24 μm. The laser beam moves from left to right. These 3D temperature clips are located at the middle of the gap.

3.3 Molten pool characteristic and pore generation

As the joint quality is affected by the stabilities of the molten pool and keyhole, in this part, the characteristic of the molten pool and bubble formation are studied. The depth of molten pool is plotted in **Fig. 13** and the profiles at specific points are also displayed.

In the initial stable growth stage of molten pool depth, the larger the gap width, the greater the depth under the same moment, which can be attributed to the gap filling effect of melt dropping down. It can be seen from the enlarged picture in **Fig. 13** (b) that in the first stage of the overall increase in the depth, there are some small fluctuation points (A, B) in the case of 12 μm and 16 μm. This is because gap intensifies the heat dissipation and solidification dominates, resulting in the depth decreasing. Due to the heat accumulation, the frozen region remelts and the depth rises, indicating that the existence of gap disturbs the molten pool. As the gap filling leads to the elongation of molten pool tip, a thin region between keyhole wall and fusion line was induced (**Fig. 8**). Under the dual action of gap disturbance and keyhole fluctuation, the case with largest gap width starts to solidify in the first place, decreasing the molten pool depth, and the stable growth stage ends. The smaller the gap, the larger the depth achieved in the first stage. This can be attributed to the low heat dissipation and large heat accumulation. The depth for 0μm is lower than that of 8μm, because gap = 8μm possesses the advantages of small heat dissipation and gap filling effect, resulting in a larger depth. A and B represent the fluctuation of melt pool depth caused by the large gap. C-F indicate the perturbation to the melt pool due to the keyhole instability in all cases, leading to a sharp change in the depth of molten pool. The larger the gap, the earlier the perturbation occurs. Although the existence of gap also has an effect on the depth, the change is smaller.

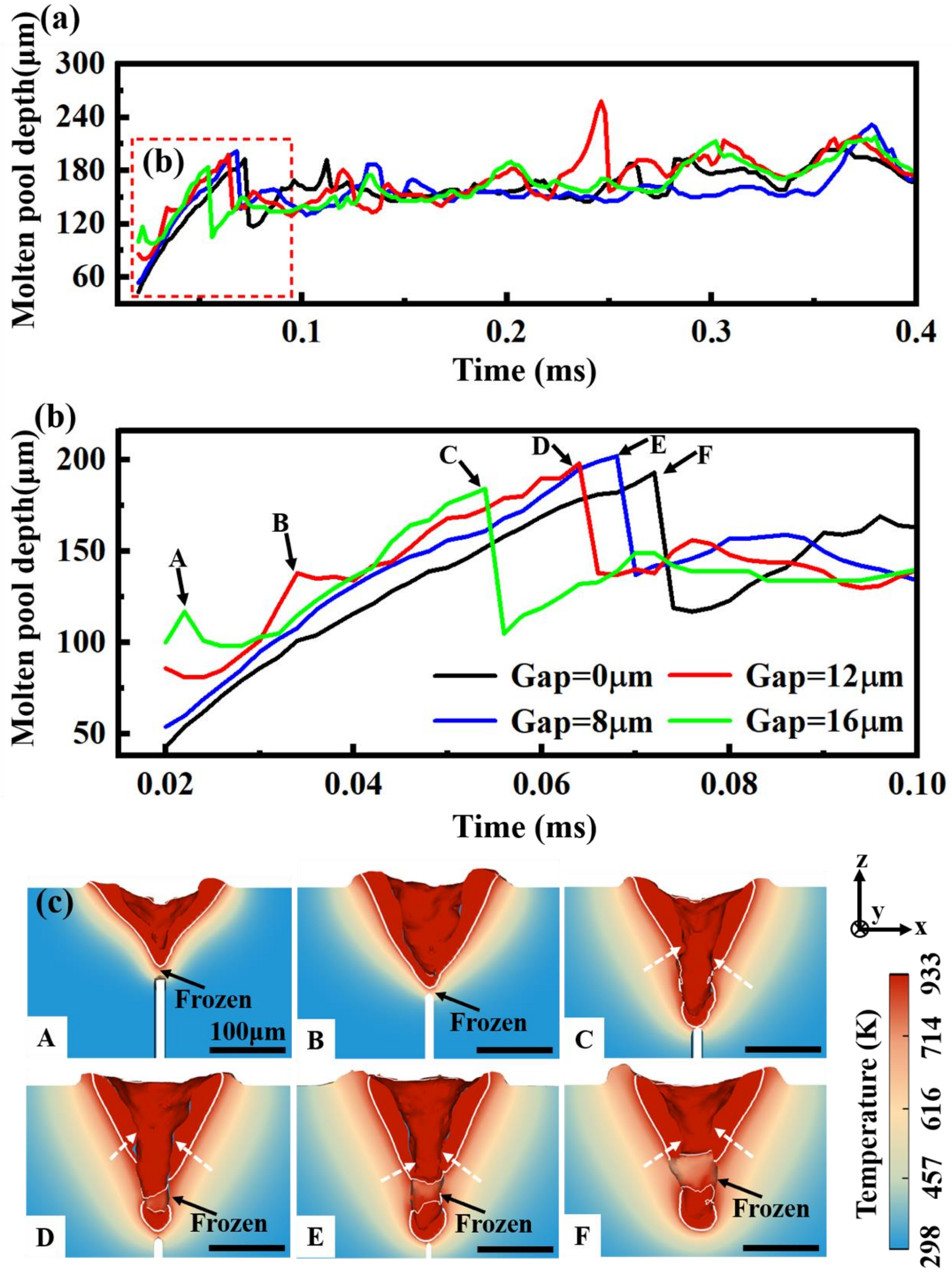

Fig. 13 (a) Depth of molten pool with different gap values (0-16 μm) and (b) the enlarged part in the dotted box. (c) The molten pool profiles in the points of A-F. A and B represent the fluctuation of melt pool depth caused by the large gap; C-F indicate the perturbation to the melt pool due to the keyhole instability in all cases, resulting in great change in depth. The white dotted arrows indicate the necking.

As the moving speed of the laser in this model is slow (16.7 mm·s^{-1}), the generated pores were mostly captured. Note that the simulation for larger number of pores in this welding model is limited by our current disk memory. Here, we can still determine the effect of gap on pore formation by the definition of bubble generation frequency, namely, the bubble formation counts within one second.

Fig. 14 shows there is little difference in the bubble formation frequency in the cases of 0 μm, 8 μm and 12 μm. When the gap increases to 16 μm, the frequency increases substantially. It is because of the special phenomenon of melt dropping down to fill the gap in laser butt welding. Therefore, the generation of bubble depends on two aspects. One is the velocity of the fluid flow. The more vigorous the flow, the easier it is to generate pores. The other is the depth of gap filling. The greater the downward filling, the more unstable the molten pool, and the higher chance to form a bubble. As shown in **Fig. 12**, when the gap value is greater than 20 μm, the fluid falls down and cannot even form a molten pool. In the case of 0 μm, there is no gap filling effect, and the fluid velocity at the molten pool bottom is large, which causes bubbles due to the fluctuation of the keyhole. As for the case of 8 μm, it possesses the advantages of low heat dissipation and gap filling. Compared to 0 μm, the velocity decreases while the melt pool depth increases. Under the effect of keyhole fluctuation and gap disturbance, the frequency increases somewhat. In the case of 12 μm, despite of the increased molten pool depth, the bubble frequency decreases slightly, which may be related to the further reduced velocity compared to 8 μm. When it comes to the case of 16 μm, the frequency is still high under the condition of large heat loss, which can be attributed to the disturbance caused by the gap. Moreover, the gap filling effect results in an elongated tip, which is likely to cause insufficient feeding at the bottom of the keyhole to form pores. All in all, gap will disturb the stability of molten pool and promote pore generation despite the heat loss.

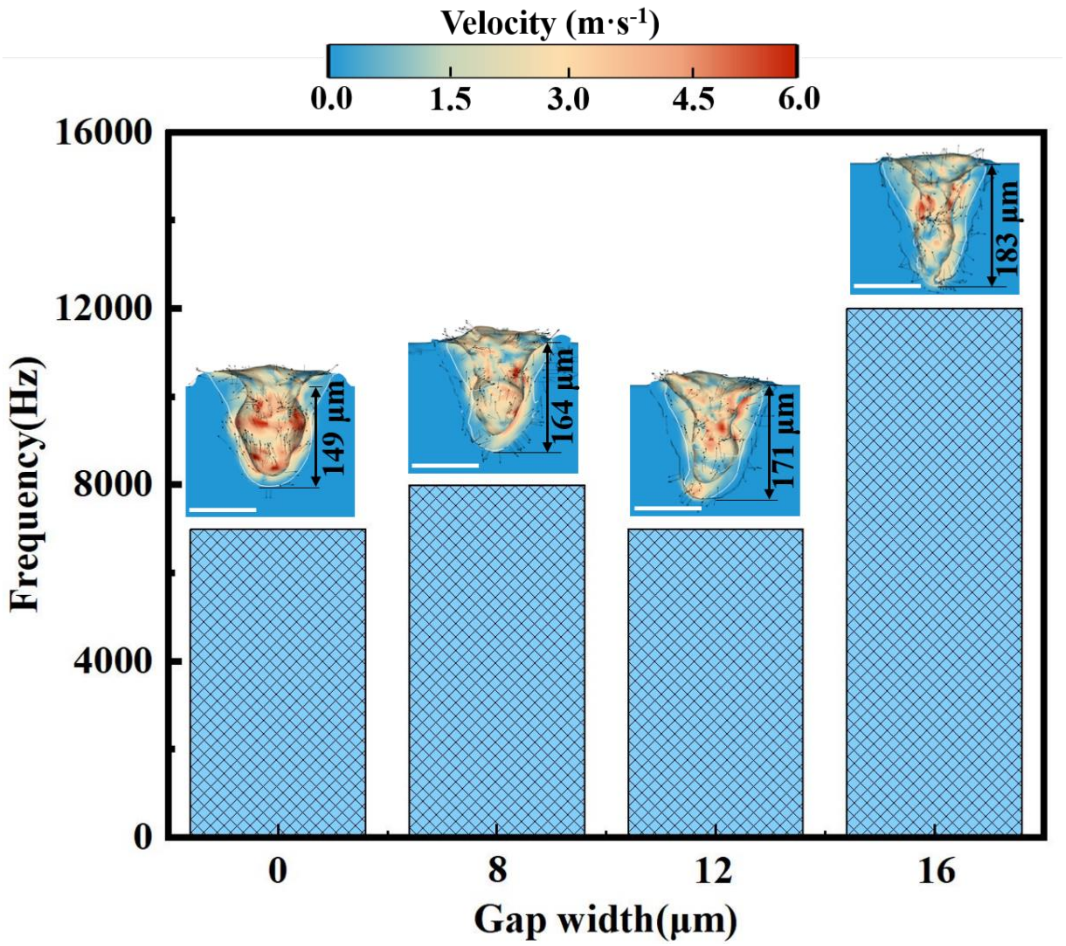

Fig. 14 Frequency of bubble generation with different gap values. The inserts show the fluid flow strength and gap filling degree corresponding to the gap below. It indicates strong flow for 0 μm, strong flow and weak downward filling for 8 μm, weak flow and weak downward filling for 12 μm, weak flow and strong downward filling for 16 μm. The scale bar is 100 μm.

4. Conclusion

In this paper, we developed a thermal-mechanistic-fluid coupled model to investigate the gap filling mechanism in laser butt welding of aluminum and the effects of gap on the molten pool characteristic and bubble generation. Our simulation model provided in-depth understanding of the experimental phenomenon of gap filling and bubble evolution obtained by in-situ X-ray imaging. Besides, the strategy to reduce the bubble defect in laser butt welding is suggested. The following key conclusions can be drawn:

(1) The metal melts and fills the gap due to the gravity and recoil pressure. Gap increases the heat dissipation. The competition between the solidification and melting determines the filling process and the shape of the molten pool. The gap filling effect

causes the molten pool tip to be elongated.

(2) Four phenomena appeared in sequence in the initial stage of butt welding. I. Gap filling. The melting velocity exceeds the solidification velocity, the fluid flows downward to fill the gap. II. Frozen. The solidification velocity dominates and the molten pool bottom solidifies. III. Remelt. Heat accumulation results in the melting process prevailing and the fluid continuously flows downward. IV. Bubble formation. Necking occurs and promotes the keyhole fluctuation. Coupled with the tip elongated effect, a bubble generates at the bottom of the keyhole.

(3) In the initial stable growth stage of the molten pool, the larger the gap width, the deeper the molten pool, all of which is caused by the downward flow that fills the gap. The sharp change of keyhole depth is due to the formation of necking, while the small fluctuation of keyhole depth with larger gap values results from the gap disturbance. The larger the gap, the earlier the gap perturbation occurs.

(4) The bubble formation depends on two aspects in laser butt welding due to its unique phenomenon of melt dropping down to fill the gap. One is the degree of the fluid flow and the other is gap filling. There is no big difference in the bubble formation frequency when the gap is no more than 12 μm. When it increases to 16 μm, the frequency increases substantially despite of the great heat loss. As the gap width exceeds 20 μm, a continuous melt pool cannot be formed due to the fluid dropping down, which is detrimental to the welding quality.

(5) In summary, it is proposed to minimize the gap width, such as reducing the surface roughness, increasing the clamping force, and so on, to improve the joint quality in the actual laser butt welding process.

Acknowledgements

This work is sponsored by National Natural Science Foundation of China (52004160 and 52075327), Shanghai Sailing Program (20YF1419200), Natural Science Foundation of Shanghai (20ZR1427500) and Major Science and Technology Project of Huaibei (Z2020001). Chu Lun Alex Leung acknowledges financial support from the EPSRC MAPP Future Manufacturing Hub (EP/P006566/1, www.mapp.ac.uk), Manufacturing by Design (EP/W003333/1), Made Smarter Innovation – Materials Made Smarter Research Centre (EP/V061798/1); Data-driven, Reliable, Effective Additive Manufacturing using multi-BEAM technologies (EP/W037483/1), and Performance-driven design of aluminium alloys for additive manufacturing (PAAM) (EP/W006774/1).

Reference

[1] H. Gu, T. Väistö, L. Li, Numerical and experimental study on the molten pool dynamics and fusion zone formation in multi-pass narrow gap laser welding, Optics & Laser Technology, 126 (2020).

[2] S. Li, G. Chen, M. Zhang, Y. Zhou, Y. Zhang, Dynamic keyhole profile during high-power deep-penetration laser welding, Journal of Materials Processing Technology, 214 (2014) 565-570.

[3] H. Wang, Y. Zhang, X. Lai, Effects of interfaces on heat transfer in laser welding of electrical steel laminations, International Journal of Heat and Mass Transfer, 90 (2015) 665-677.

[4] C. Zhao, K. Fezzaa, R.W. Cunningham, H. Wen, F. De Carlo, L. Chen, A.D. Rollett, T. Sun, Real-time monitoring of laser powder bed fusion process using high-speed X-ray imaging and diffraction, Sci Rep, 7 (2017) 3602.

[5] H. Wang, M. Nakanishi, Y. Kawahito, Dynamic balance of heat and mass in high power density laser welding, Opt Express, 26 (2018) 6392-6399.

[6] C.L.A. Leung, S. Marussi, R.C. Atwood, M. Towrie, P.J. Withers, P.D. Lee, In situ X-ray imaging of defect and molten pool dynamics in laser additive manufacturing, Nat Commun, 9 (2018) 1355.

[7] Y. Huang, T.G. Fleming, S.J. Clark, S. Marussi, K. Fezzaa, J. Thiyagalingam, C.L.A. Leung, P.D. Lee, Keyhole fluctuation and pore formation mechanisms during laser powder bed fusion additive manufacturing, Nat Commun, 13 (2022) 1170.

[8] S. Karagadde, C.L.A. Leung, P.D. Lee, Progress on In Situ and Operando X-ray Imaging of Solidification Processes, Materials (Basel), 14 (2021).

[9] C.L.A. Leung, D. Luczyniec, E. Guo, S. Marussi, R.C. Atwood, M. Meisnar, B. Saunders, P.D. Lee, Quantification of Interdependent Dynamics during Laser Additive Manufacturing Using X-Ray Imaging Informed Multi-Physics and Multiphase Simulation, Adv Sci (Weinh), DOI 10.1002/advs.202203546(2022) e2203546.

[10] M. Miyagi, X. Zhang, Investigation of laser welding phenomena of pure copper by x-ray observation system, Journal of Laser Applications, 27 (2015).

[11] Y. Kawahito, Y. Uemura, Y. Doi, M. Mizutani, K. Nishimoto, H. Kawakami, M. Tanaka, H. Fujii, K. Nakata, S. Katayama, Elucidation of effect of welding speed on melt flows in high-brightness and high-power laser welding of stainless steel on basis of three-dimensional X-ray transmission in-situ observation, Quarterly Journal of the Japan Welding Society, 33 (2015) 13-19.

[12] Y. Kawahito, M. Mizutani, S. Katayama, High quality welding of stainless steel with 10 kW high power fibre laser, Science and Technology of Welding and Joining, 14 (2013) 288-294.

[13] A. Heider, J. Sollinger, F. Abt, M. Boley, R. Weber, T. Graf, High-Speed X-Ray Analysis of Spatter Formation in Laser Welding of Copper, Physics Procedia, 41 (2013) 112-118.

[14] A. Matsunawa, M. Mizutani, S. Katayama, N. Seto, Porosity formation mechanism and its prevention in laser welding, Welding International, 17 (2003) 431-437.

[15] S. Katayama, A. Matsunawa, Microfocused X-ray transmission real-time observation of laser welding phenomena, Welding International, 16 (2002) 425-431.

[16] X. Chen, A. Matsunawa, T. Fujioka, N. Seto, J.-D. Kim, A. Matsunawa, M. Mizutani, S. Katayama, Dynamics of keyhole and molten pool in high-power CO 2 laser welding, High-Power Lasers in Manufacturing, 2000.

[17] Y. Kawahito, H. Wang, In-situ observation of gap filling in laser butt welding, Scripta Materialia, 154 (2018) 73-77.

[18] J. Hensel, M. Köhler, L. Uhlenberg, J.D.e. Castro, K. Dilger, M. Faß, J. Baumgartner, Laser welding of 16MnCr5 butt welds with gap: resulting weld quality and fatigue strength assessment,

Welding in the World, 66 (2022) 1867-1881.

[19] S. Chen, Y. Zhao, S. Tian, Y. Gu, X. Zhan, Study on keyhole coupling and melt flow dynamic behaviors simulation of 2219 aluminum alloy T-joint during the dual laser beam bilateral synchronous welding, Journal of Manufacturing Processes, 60 (2020) 200-212.

[20] W.-I. Cho, S.-J. Na, C. Thomy, F. Vollertsen, Numerical simulation of molten pool dynamics in high power disk laser welding, Journal of Materials Processing Technology, 212 (2012) 262-275.

[21] H. Wang, Y. Zhang, K. Chen, Modeling of Temperature Distribution in Laser Welding of Lapped Martensitic Steel M1500 and Softening Estimation, Journal of Manufacturing Science and Engineering, 138 (2016).

[22] L. Li, G. Peng, J. Wang, J. Gong, S. Meng, Numerical and experimental study on keyhole and melt flow dynamics during laser welding of aluminium alloys under subatmospheric pressures, International Journal of Heat and Mass Transfer, 133 (2019) 812-826.

[23] Y. Ai, P. Jiang, C. Wang, G. Mi, S. Geng, Experimental and numerical analysis of molten pool and keyhole profile during high-power deep-penetration laser welding, International Journal of Heat and Mass Transfer, 126 (2018) 779-789.

[24] M. Sohail, S.-W. Han, S.-J. Na, A. Gumenyuk, M. Rethmeier, Numerical investigation of energy input characteristics for high-power fiber laser welding at different positions, The International Journal of Advanced Manufacturing Technology, 80 (2015) 931-946.

[25] S. Pang, W. Chen, J. Zhou, D. Liao, Self-consistent modeling of keyhole and weld pool dynamics in tandem dual beam laser welding of aluminum alloy, Journal of Materials Processing Technology, 217 (2015) 131-143.

[26] W. Tan, N.S. Bailey, Y.C. Shin, Investigation of keyhole plume and molten pool based on a three-dimensional dynamic model with sharp interface formulation, Journal of Physics D: Applied Physics, 46 (2013).

[27] H. Wang, Y. Shi, S. Gong, Effect of pressure gradient driven convection in the molten pool during the deep penetration laser welding, Journal of Materials Processing Technology, 184 (2007) 386-392.

[28] M.A.B. Cook P Simulation of melt pool behaviour during additive manufacturing: Underlying physics and progress, Additive Manufacturing, 31 (2020).

[29] S. Pang, K. Hirano, R. Fabbro, T. Jiang, Explanation of penetration depth variation during laser welding under variable ambient pressure, Journal of Laser Applications, 27 (2015).

[30] H. Wang, Y. Zou, Microscale interaction between laser and metal powder in powder-bed additive manufacturing: Conduction mode versus keyhole mode, International Journal of Heat and Mass Transfer, 142 (2019).

[31] R. Lin, H.-p. Wang, F. Lu, J. Solomon, B.E. Carlson, Numerical study of keyhole dynamics and keyhole-induced porosity formation in remote laser welding of Al alloys, International Journal of Heat and Mass Transfer, 108 (2017) 244-256.

[32] L. Guo, H. Wang, H. Liu, Y. Huang, Q. Wei, C.L.A. Leung, Y. Wu, H. Wang, Understanding keyhole induced-porosities in laser powder bed fusion of aluminum and elimination strategy, International Journal of Machine Tools and Manufacture, 184 (2023).

[33] A.A. Martin, N.P. Calta, S.A. Khairallah, J. Wang, P.J. Depond, A.Y. Fong, V. Thampy, G.M. Guss, A.M. Kiss, K.H. Stone, C.J. Tassone, J. Nelson Weker, M.F. Toney, T. van Buuren, M.J. Matthews, Dynamics of pore formation during laser powder bed fusion additive manufacturing, Nat Commun, 10 (2019) 1987.

[34] H. Wang, M. Nakanishi, Y. Kawahito, Effects of welding speed on absorption rate in partial and full penetration welding of stainless steel with high brightness and high power laser, Journal of Materials Processing Technology, 249 (2017) 193-201.